Available online at www.sciencedirect.com
ScienceDirect
Journal of Sound and Vibration 317 (2008) 273–293
JOURNAL OF SOUND AND VIBRATION
www.elsevier.com/locate/jsvi

Whirl and whip instabilities in rotor-bearing system considering a nonlinear force model

Helio Fiori de Castro[a], Katia Lucchesi Cavalca[a,*], Rainer Nordmann[b]

[a]Department of Mechanical Design—Unicamp, Postal Box 6122, 13083-970 Campinas, SP, Brazil
[b]Department of Mechatronics in Mechanical Engineering, TU-Darmstadt, Petersenstrasse. 30, D-64287 Darmstadt, Germany

Received 17 April 2007; received in revised form 25 February 2008; accepted 27 February 2008
Handling Editor: P. Davies
Available online 8 April 2008

Abstract

Linear models and synchronous response are generally adequate to describe and analyze rotors supported by hydrodynamic bearings. Hence, stiffness and damping coefficients can provide a good model for a wide range of situations. However, in some cases, this approach does not suffice to describe the dynamic behavior of the rotor-bearing system. Moreover, unstable motion occurs due to precessional orbits in the rotor-bearing system. This instability is called "oil whirl" or "oil whip". The oil whirl phenomenon occurs when the journal bearings are lightly loaded and the shaft is whirling at a frequency close to one-half of rotor angular speed. When the angular speed of the rotor reaches approximately twice the natural frequency (first critical speed), the oil whip phenomenon occurs and remains even if the rotor angular speed increases. Its frequency and vibration mode correspond to the first critical speed. The main purpose of this paper is to validate a complete nonlinear solution to simulate the fluid-induced instability during run-up and run-down. A flexible rotor with a central disk under unbalanced excitation is modeled. A nonlinear hydrodynamic model is considered for short bearing and laminar flow. The effects of unbalance, journal-bearing parameters and rotor arrangement (vertical or horizontal) on the instability threshold are verified. The model simulations are compared with measurements at a real vertical power plant and a horizontal test rig.

1. Introduction

Studies of the characteristics of rotor-bearing systems are necessary in the design of rotating systems and their industrial applications, and for the diagnosis of system malfunctions. Mathematical models have been developed to represent real machines with considerable confidence. Research has also focused on determining better models of rotating machinery, such as turbogenerators and multistage pumps, which are horizontal rotating machines with high load capacity. Childs et al. [1] proposed a nonlinear hydrodynamic force model, based on journal bearing impedance descriptions, which can be used to analyze stability but not to simulate

*Corresponding author.
E-mail addresses: heliofc@fem.unicamp.br (H.F. de Castro), katia@fem.unicamp.br (K.L. Cavalca), nordmann@mim.tu-darmstadt.de (R. Nordmann).

0022-460X/$ - see front matter © 2008 Elsevier Ltd. All rights reserved.
doi:10.1016/j.jsv.2008.02.047

Nomenclature

C	bearing radial clearance
$[C]$	damping matrix of the system
D	bearing diameter
e	unbalanced mass eccentricity
E	Young's modulus
F	auxiliary hydrodynamic force function
$\{F_h\}$	nonlinear hydrodynamic forces
$\{F_u\}$	unbalanced forces
G	auxiliary hydrodynamic force function
$[G]$	gyroscopic matrix of the system
h	dimensionless oil film thickness
H	oil film thickness
J_z	polar moment of inertia
$[K]$	stiffness matrix of the system
L	bearing length
L_e	shaft element length
m	unbalanced mass
$[M]$	mass matrix of the system
p	dimensionless oil pressure distribution
P	oil pressure distribution
$\{q\}$	generalized coordinates.
Q	dimensionless unbalanced magnitude
R	bearing radius
T_z	rotor torque
V	auxiliary hydrodynamic force function
$\{W\}$	rotor weight
x	radial dimensionless displacement of the journal in the bearing
X	radial displacement of the journal in the bearing
y	radial dimensionless displacement of the journal in the bearing
Y	radial displacement of the journal in the bearing
z	axial dimensionless displacement of the rotor
Z	axial displacement of the rotor
$\bar{Z}$	coordinate reference
α	auxiliary hydrodynamic force function
β	proportional damping coefficient related to stiffness
μ	dynamic viscosity of oil
v	cylindrical coordinate of the bearing
ρ	mass density
φ	rotation angle of the rotor

fluid-induced instability. Capone [2,3] developed numerical simulations to study cylindrical hydrodynamic bearings, obtaining the orbits of the shaft in the bearings based on a nonlinear hydrodynamic force model.

Other researchers have investigated the speed-dependent behavior of bearing characteristics. Tiwari et al. [4] developed an identification algorithm for the characterization of bearing dynamics using unbalanced response measurements for multidegree-of-freedom flexible rotor-bearing systems. Sinha et al. [5] proposed an identification method to estimate the static load on the fluid bearings of a flexible machine from rundown data. This is an important practical problem, because static load strongly influences the bearing's dynamic characteristics.

Linear journal-bearing models are normally used to simulate rotor-bearing systems. However, linear models are not ideal to represent real rotating systems in certain situations. In such cases, nonlinear models should be employed to better represent real systems [6–9].

The interaction between the rotating system and the oil film in a hydrodynamic bearing causes unstable dynamic behavior [10], which is characterized by a subsynchronous forward precessional vibration. These dynamic behaviors are called oil whirl and oil whip [7,11–14].

These instabilities are a kind of self-exciting vibration of a rotor-bearing system. The oil whirl is a subsynchronous precessional movement that vibrates at a frequency close to half of the rotation speed. When the rotation speed reaches twice the first natural frequency, the self-excited vibration frequency remains constant and close to the first resonance frequency. This new behavior is the oil whip instability. Oil whip instability, in particular, can be severely harmful to the rotor-bearing system. The journal's amplitude is limited by the journal bearing clearance, but the shaft vibration amplitude may become very high, since it vibrates at the natural frequency [11]. The two fluid-induced instability effects can be associated to the bearing stiffness and the shaft stiffness. If the journal is close to the bearing center, the bearing stiffness is much lower than the shaft stiffness. In that case, the system stiffness is controlled by the bearing stiffness and the fluid-induced instability occurs due to oil whirl [15,16]. On the other hand, when the journal is too close to the

bearing wall, the bearing stiffness is much higher than the shaft stiffness. In that case, the system stiffness is similar to the shaft stiffness and the instability vibration is caused by the oil whip, which is related to the bending mode of the rotor system [7].

To reduce the effects of this particular dynamic behavior, some authors have been studying control methods to reduce oil instability [17].

Jing et al. [18,19] considered the nonlinear model proposed by Capone [2,3] to analyze the nonlinear dynamic behavior of bearings, taking into account the oil whip phenomenon, although the angular acceleration was not considered as it is in the present work.

Owing to the nonlinearities of rotating systems supported by lubricated bearings, some researchers applied nonlinear techniques to study the dynamic behavior of these systems [20–23]. These techniques were used to identify fluid-induced instabilities demonstrated by experimental results of horizontal and vertical rotors [24].

Castro et al. [7] introduced angular acceleration in the equation of motion and analyzed fluid-induced instability (oil whirl and oil whip). They found that Capone's model is able to model the rotor's dynamic behavior under fluid-induced instabilities in transient motion, thus allowing for stability analyses according to Refs. [11–14].

To continue the study started by Castro et al. [7], an analysis is made taking into account the dynamic behavior of a rotating system under the oil whirl and oil whip phenomenon, considering the influence of unbalance, rotor arrangement (vertical or horizontal rotor) and bearing parameters (L/D ratio, bearing clearance and oil viscosity) on the instability threshold. In addition, the simulated results are compared with measurements taken at a real vertical power plant and in a horizontal test rig.

2. Mathematical model

A mathematical model of a rotating system can be divided into two parts: the finite element model of the shaft and concentrated mass of the disk, and the nonlinear hydrodynamic supporting forces of the cylindrical journal bearing [2,3], which is obtained by solving the Reynolds equation for short bearings. A short journal bearing scheme and the cylindrical coordinate reference system are shown in Fig. 1.

Eq. (1) describes the pressure distribution P inside the cylindrical journal bearing, based on the solution of the Reynolds equation for the laminar flow condition:

$$\frac{\partial}{\partial v}\left(h^3\frac{\partial p}{\partial \vartheta}\right)+\left(\frac{R}{L}\right)^2\frac{\partial}{\partial z}\left(h^3\frac{\partial p}{\partial z}\right)=\frac{\partial h}{\partial \vartheta}+2\frac{\mathrm{d}h}{\mathrm{d}\tau}, \tag{1}$$

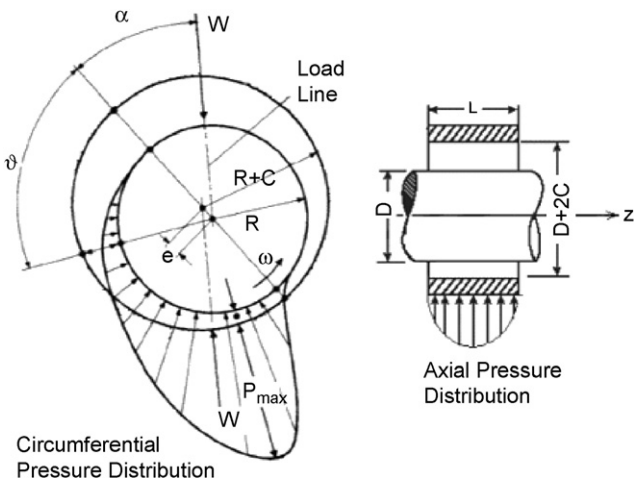

Fig. 1. Short journal-bearing scheme and coordinate reference system.

where the dimensionless parameters are

$$h=\frac{H}{C}=1-x\cos(\vartheta)-y\sin(\vartheta),\ z=\frac{Z}{L},\ x=\frac{X}{C},\ y=\frac{Y}{C},\ \tau=\dot{\varphi}t,\ p=\frac{P}{p_0}\ \text{and}\ p_0=6\mu\dot{\varphi}\left(\frac{R}{C}\right)^2.$$

The solution of Eq. (1) considers the axial gradient ($\partial p/\partial z$) due to axial losses of lubricating fluid in a short journal bearing, neglecting the pressure gradient in the angular direction ($\partial p/\partial\vartheta$). The bearing parameters are radial clearance C, bearing length L, bearing radius R and oil viscosity μ. The dimensionless oil film thickness h, dimensionless time τ, rotor angular speed $\dot{\varphi}$, and dimensionless journal displacement in horizontal x, vertical y and axial z directions are also considered.

The fluid is considered incompressible and the viscosity is assumed to be constant across the fluid. Half Sommerfeld solution is applied and the cavitation effect is neglected, considering null pressure for negative values of pressure distribution. Thus, the complete theoretical solution of the differential equation under these hypotheses is given by

$$p(\vartheta,z)=\frac{1}{2}\left(\frac{L}{D}\right)^2\left[\frac{(x-2\dot{y})\sin(\vartheta)-(y+2\dot{x})\cos(\vartheta)}{(1-x\cos(\vartheta)-y\sin(\vartheta))^3}\right](4z^2-1). \tag{2}$$

In order to determine the hydrodynamic force Fh generated by the distribution of the oil film pressure on the shaft, the differential contact area ($\mathrm{d}A=R\,\mathrm{d}\vartheta L\,\mathrm{d}z$) is considered in the integration, resulting in Eq. (3):

$$\{F_h\}=\begin{Bmatrix}F_{hx}\\F_{hy}\end{Bmatrix}=-\mu\omega\left(\frac{R^2}{C^2}\right)\left(\frac{L^2}{D^2}\right)(RL)\frac{[(x-2\dot{y})^2+(y+2\dot{x})^2]^{1/2}}{(1-x^2-y^2)}\begin{Bmatrix}3xV(x,y,\alpha)-\sin(\alpha)G(x,y,\alpha)-2\cos(\alpha)F(x,y,\alpha)\\3yV(x,y,\alpha)-\cos(\alpha)G(x,y,\alpha)-2\sin(\alpha)F(x,y,\alpha)\end{Bmatrix}, \tag{3}$$

where the functions V, G, F and α are, respectively, given in Eqs. (4)–(7):

$$V(x,y,\alpha)=\frac{2+(y\cos(\alpha)-x\sin(\alpha))G(x,y,\alpha)}{(1-x^2-y^2)}, \tag{4}$$

$$G(x,y,\alpha)=\int_{\alpha}^{\alpha+\pi}\frac{\mathrm{d}\upsilon}{(1-x\cos(\upsilon)-y\sin(\upsilon))}=\frac{\pi}{\sqrt{1-x^2-y^2}}-\frac{2}{\sqrt{1-x^2-y^2}}\tan^{-1}\left(\frac{y\cos(\alpha)-x\sin(\alpha)}{\sqrt{1-x^2-y^2}}\right), \tag{5}$$

$$F(x,y,\alpha)=\frac{(x\cos(\alpha)+y\sin(\alpha))}{(1-x^2-y^2)}, \tag{6}$$

$$\alpha=\tan^{-1}\left(\frac{y+2\dot{x}}{x-2\dot{y}}\right)-\frac{\pi}{2}\mathrm{sign}\left(\frac{y+2\dot{x}}{x-2\dot{y}}\right)-\frac{\pi}{2}\mathrm{sign}(y+2\dot{x}). \tag{7}$$

The horizontal rotor scheme is shown in Figs. 2a and b and its finite element model is illustrated in Fig. 2c. The differential equation of motion is given by Eq. (8), which takes into account the hydrodynamic force $\{F_h\}$ given in Eq. (3), the unbalanced forces $\{F_u\}$, the rotor weight $\{W\}$ and the generalized coordinates of the flexible rotor $\{q\}^{\mathrm{T}}=\{x_1,\ y_1,\ \ldots,\ x_3,\ y_3,\ \ldots\ x_6,\ y_6,\ \ldots,\ x_9,\ y_9,\ \ldots\ x_{11},\ y_{11}\}$, which consider all the degrees of freedom of the rotating system, including the journal displacement in each bearing. If a vertical rotor is assumed, the rotor weight is not considered:

$$[M]\{\ddot{q}\}+[C][\dot{q}]+[K]\{q\}=\{F_u\}+\{F_h\}-\{W\}. \tag{8}$$

In order to determine the mass $[M]$ and stiffness $[K]$ matrices, a finite element method is used, considering the shaft and the concentrated mass of the rotor [25,26].

The shaft damping matrix $[C]$ contains a first part proportional to the stiffness matrix and a second part with the gyroscopic effects ($[C]=\beta[K]+\dot{\varphi}[G]$). The gyroscopic matrix $[G]$ is also obtained by a finite element method.

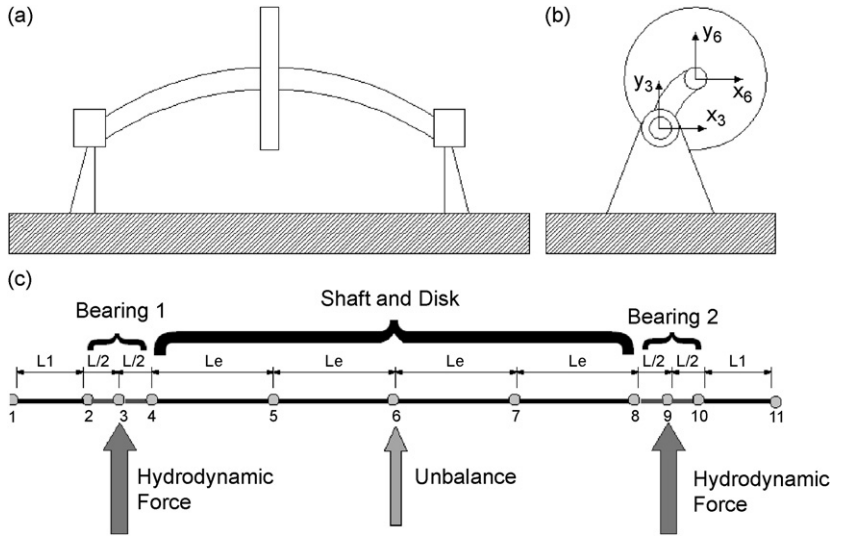

Fig. 2. Horizontal rotor: (a) physical model; (b) physical model—cross-section; (c) finite element model.

Table 1
Material properties for simulation

Material property	Value
Young's modulus, E	2.067×10^{11} Pa
Density, ρ	7800 kg/m^3
Proportional coefficient related to stiffness, β	25×10^{-5}

The system excitation force is due to the unbalanced mass m and its eccentricity e, expressed in Eq. (9):

$$\{F_u\} = me\begin{Bmatrix} \ddot{\varphi}\sin\varphi + \dot{\varphi}^2\cos\varphi \\ \ddot{\varphi}\sin\varphi + \varphi\dot{\varphi}^2\cos\varphi \end{Bmatrix}. \tag{9}$$

To consider the angular acceleration $\ddot{\varphi}$ of the rotating system, Eq. (10) correlates the drive-motor input torque T_Z with the rotation of the system [27], where J_z is the polar moment of inertia. This equation is obtained by Lagrange's equation and considers the coupling between torsional and lateral vibrations:

$$J_z\ddot{\varphi} \cong T_z + me(\sin\varphi\ddot{x} - \cos\varphi\ddot{y} + \dot{\varphi}\dot{x}\cos\varphi + \dot{\varphi}\dot{y}\sin\varphi). \tag{10}$$

However, this coupling is considerably weak and can be neglected, as indicated by Childs [14]. Eq. (10) is therefore reduced to Eq. (11):

$$J_z\ddot{\varphi} \cong T_z. \tag{11}$$

The solution of the equation of motion is obtained using numerical methods. The Newmark integration method was chosen here because it is a robust algorithm to solve nonlinear equations in the time domain.

3. Simulation results

3.1. Simulation data

Considering a constant angular acceleration, the length of the four elements between the bearings is $L_e = 0.1450$ m, the shaft diameter is 0.012 m and the centered disk diameter and length are 0.095 and 0.043 m, respectively. Simulations were done varying the unbalance and the journal-bearing parameters, as well as the rotor position (horizontal or vertical). Table 1 lists the material properties considered in the model. A low

proportional structural damping coefficient β was assumed in order to highlight the effects studied in this work. In all the simulations, the system's dynamic rundown rather than runup behavior is analyzed, since the latter may be associated with other phenomena such as the inertial effect of the oil whip.

The dynamic behavior of a rotor supported by journal bearings is important in the design stage. In predictive maintenance, one can also use the prediction of the dynamic behavior to diagnose failure. The complete model of the system consists of a linear finite element model for the rotor and a nonlinear model for the bearings. Before beginning the numerical simulations of the system parameters, the congruence of the results of the theoretical model and the experimental test rig is ascertained. The influence of design variables such as unbalance and bearing parameters can be then simulated. The influence of a vertical or horizontal rotor was also taken into account.

3.2. Horizontal and vertical rotor

First a comparison is made between the horizontal and vertical rotor. Table 2 presents the properties of the unbalanced moment (*me*) and the journal bearing. Fig. 3 shows the displacement of the rotor in the bearing for the horizontal and vertical case in the x and y directions. Waterfall plots must be drawn with the rotor under acceleration in order to observe the dynamic behavior in the frequency domain. This type of diagram

Table 2
Parameters for the comparison of horizontal and vertical behavior

Unbalance moment *me*	2×10^{-5} kg m
Bearing clearance, C	90 μm
Bearing diameter, D	0.031 m
Bearing length, L	0.010 m
Oil viscosity, μ	0.04 Pa s

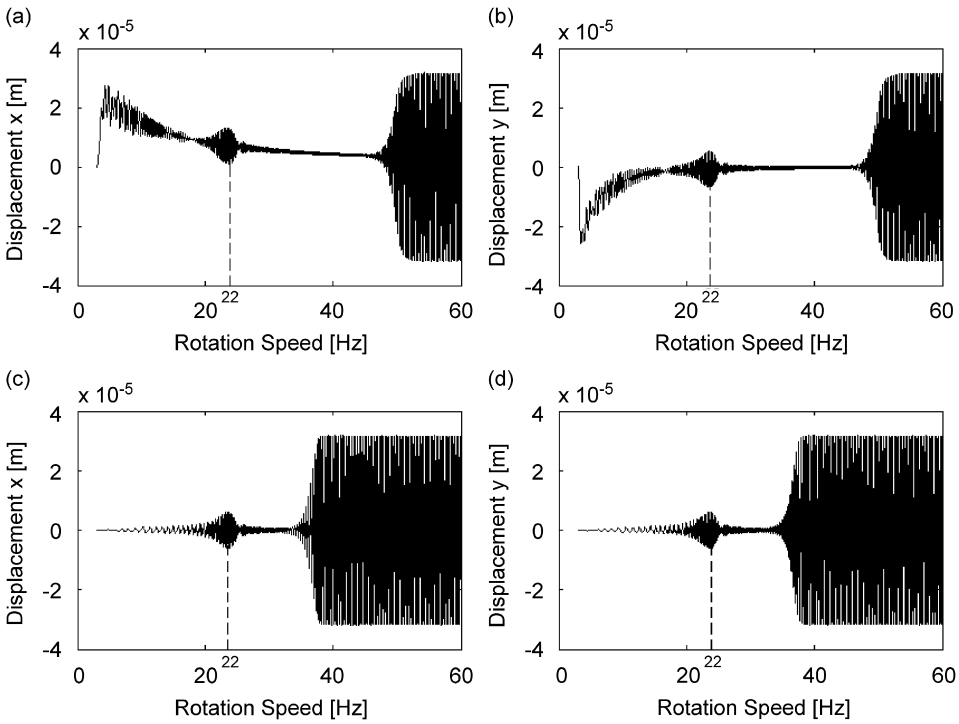

Fig. 3. (a) Displacement x—horizontal rotor, (b) displacement y—horizontal rotor, (c) displacement x—vertical rotor; (d) displacement y—vertical rotor.

correlates the rotating speed, signal magnitude and frequency spectrum, indicating if the precessional vibration is dominated by a synchronous or asynchronous vibration or even by a combination of them. Considering the displacements in the bearing, waterfall plots are generated for each case, as shown in Fig. 4a for a horizontal rotor and in Fig. 4b for a vertical rotor.

The resonance frequency of the rotor is close to 22 Hz, as illustrated in Fig. 3, which indicates that precessional vibration increases in both cases when the rotation speed approaches 22 Hz. Fig. 4 shows a similar result because both cases (horizontal and vertical) present a 1.0 × increase in vibration amplitude at a frequency of 22 Hz.

In the vertical rotor, the shaft vibrates around the geometric center of the bearing. However, at low rotational speeds, this equilibrium point in the horizontal rotor is not in the bearing's geometric center, as indicated in Figs. 3a and b. The amplitude at zero Hz in the waterfall plot of the horizontal rotor (Fig. 4a) represents the equilibrium position of the shaft. This position is far from the bearing center at lower rotation speeds, but close to the center in the oil whip region (above 45 Hz).

To link the waterfall diagrams (Fig. 4) to the dynamic behavior of the rotor-bearing system, some rotation speed intervals are analyzed. In the horizontal rotor, the first region occurs before the resonance frequency, below 20 Hz. The displacements shift towards the center of the bearing center as the rotation speed increases, as illustrated in Figs. 3a and b. The second region occurs between 20 and 25 Hz, when the synchronous vibration assumes higher values and the rotor crosses over the resonance. The vibration in the third region located above the resonance (between 25 and 45 Hz) is of lower amplitude and the oil whirl precessional vibration is not evident here. One of the reasons for this behavior is the influence of the system's weight, which leads to a position of equilibrium and, hence, to stable motion. The fourth region, characterized by the highest vibration amplitude caused by the oil whip, occurs above 45 Hz. Here, the shaft equilibrium position is at the bearing's geometric center.

The vertical rotor displacements generally occur around the center of the bearing, as indicated in Figs. 3c and d. Similarly to the horizontal case, four regions are also visible here: the region before the resonance frequency at 20 Hz, the resonance region between 20 and 25 Hz, the oil whirl region from 30 to 45 Hz, and the fourth region, above 45 Hz, which suffers the oil whip effect and where amplitudes increase significantly (Fig. 4b).

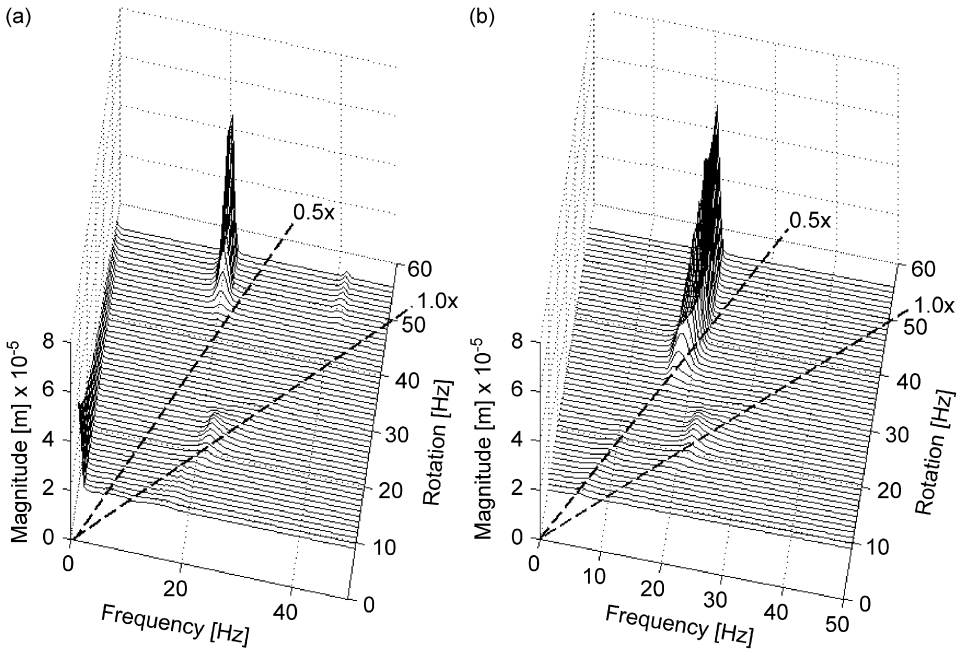

Fig. 4. Waterfall diagrams for $me = 2 \times 10^{-5}$ kg m: (a) horizontal rotor; (b) vertical rotor.

The synchronous vibration decreases above resonance in the vertical rotor, at which point the subsynchronous vibration enters into action. From 30 to 45 Hz (Fig. 4b), the vibration frequency is close to one half of rotation speed, which is characterized by oil whirl. Above 45 Hz (or twice the resonance frequency), the vibration frequency remains constant and equal to the resonance frequency (22 Hz). This is oil whip behavior. In the horizontal rotor, oil whirl is not noticeable in the same frequency range. Instead, oil whip appears at close to double the first resonance frequency (45 Hz) because the system's dynamic behavior is stable up to this frequency due to the rotor weight effect (Fig. 4a).

The main reason for the distinct behaviors of these two assemblies (horizontal and vertical) is the journal's position in the bearing. Because the journal usually closer to the bearing center in the vertical rotor, the oil whirl effect is more evident in the vertical assembly. In contrast, in the horizontal rotor, the journal vibrates around the journal's position of equilibrium in the bearing (shaft locus), which is not as close to the center of the bearing as in the vertical rotor (see Figs. 3a and b).

3.3. Unbalance influence

The influence of unbalance was investigated in the vertical rotor because the instability is more evident in this assembly. The journal-bearing parameters listed in Table 2 were taken into account in the numerical simulations.

Fig. 5 illustrates the progression of the deflection in the journal bearing as the rotation speed increases. Different unbalanced moments are considered for each curve. The analysis is aided by waterfall plots for some conditions to better illustrate this progression. The waterfall plot in Fig. 4b represents the lowest unbalanced moment ($me = 2 \times 10^{-5}$ kg m), while the waterfall plots in Figs. 6a and b show moments of greater unbalance of 5 and 7.5×10^{-5} kg m, respectively.

The subsynchronous motion ($0.5\times$) lasts longer for lower unbalanced moments, due to the weak forward synchronous vibration at $1.0\times$. When the moment of unbalance increases, the amplitude of the synchronous vibration increases and dominates the precessional motion of the rotor. When the rotation speed exceeds the first resonance frequency at 22 Hz, the precession becomes subsynchronous. Because the unbalance is higher, the beginning of subsynchronous movement shifts to higher rotational speeds, occurring even closer to double the first resonance frequency where the rotor vibrates in its natural frequency, which does not change in the frequency domain. This effect is called oil whip instability.

To analyze how unbalance affects the nonlinear behavior of the rotor-bearing system, bifurcation diagrams were drawn for 32 and 35 Hz. These two rotation speeds were chosen because instability begins in this range of frequencies and the amplitude increases significantly, as indicated in Fig. 5. Figs. 7a and b, respectively, depict

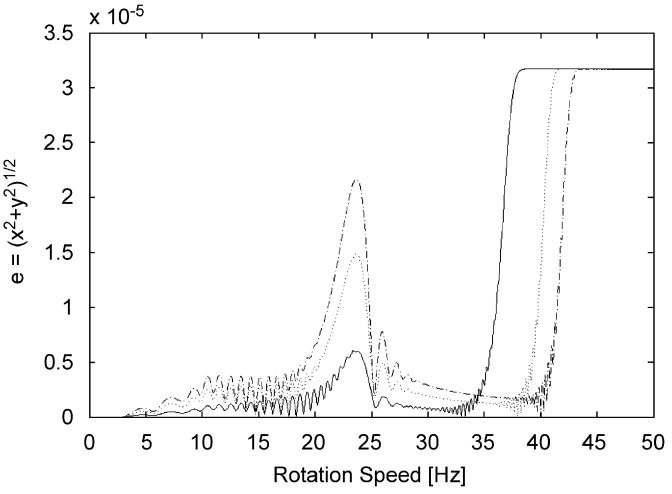

Fig. 5. Nonstationary deflection of the rotor considering several unbalanced values (solid line—$me = 2 \times 10^{-5}$ kg m; dotted line—$me = 5.0 \times 10^{-5}$ kg m; dashed line—$me = 7.5 \times 10^{-5}$ kg m).

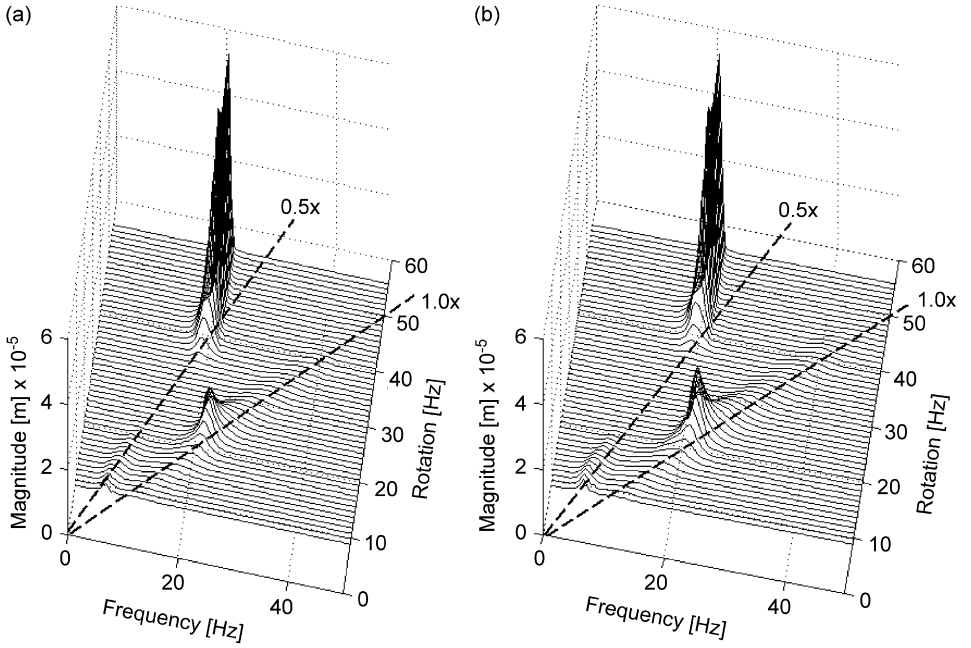

Fig. 6. Waterfall diagrams: (a) $me = 5.0 \times 10^{-5}$ kg m; (b) $me = 7.5 \times 10^{-5}$ kg m.

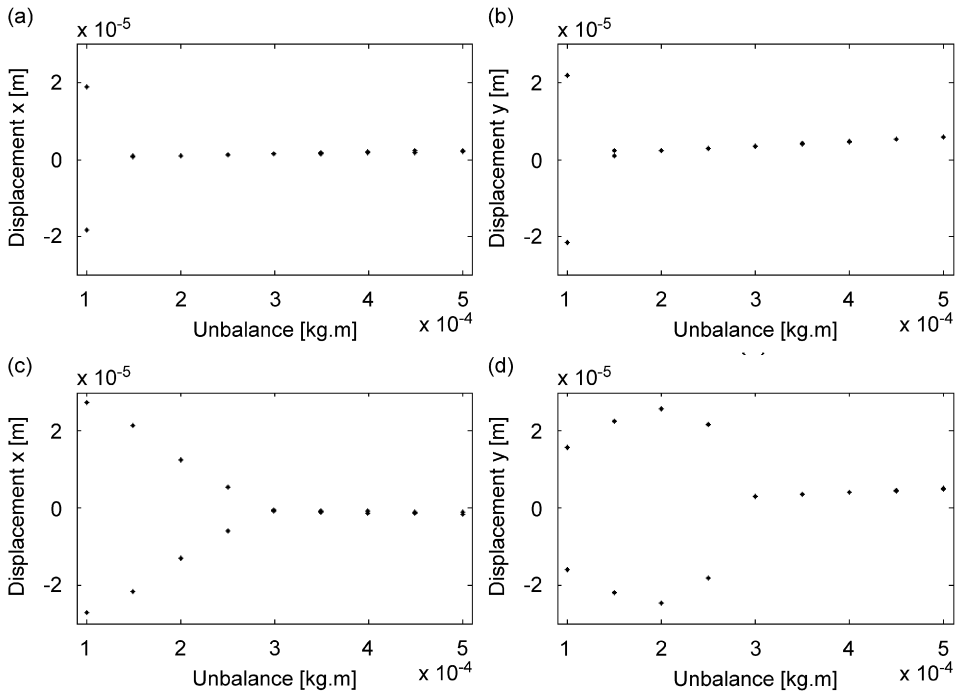

Fig. 7. (a) Bifurcation diagram for unbalance influence: (a) horizontal displacement at 32 Hz; (b) vertical displacement at 32 Hz; (c) horizontal displacement at 35 Hz; (d) vertical displacement at 35 Hz ($C = 90\,\mu$m, $L/D = 0.5$ and $\mu = 0.04$ Pa s).

bifurcation diagrams of horizontal and vertical displacement at 32 Hz, while Figs. 7c and d show these displacements at 35 Hz.

At 32 Hz, the unbalance threshold of instability is 1.5×10^{-4} kg m. A period-doubling bifurcation is encountered above this threshold, which means that there is a transition from a synchronous whirl to a

subsynchronous whirl at approximately half the rotating speed, indicating oil whirl instability [23]. Fig. 8 shows the rotor orbit and Poincaré sections. In the orbit where the unbalance is 1.0×10^{-4} kg m, the whirl is subsynchronous due to the period-doubling motion described by the Poincaré sections. The transition from period doubling to period motion is clearly visible when the unbalance is 1.5×10^{-4} kg m. At an unbalance of more than 1.5×10^{-4} kg m, the whirl is synchronous (period motion).

When the rotation speed is 35 Hz, the unbalanced threshold of instability occurs at 3×10^{-4} kg m, indicating that when the unbalance is higher, the beginning of subsynchronous movement shifts to higher rotational speeds.

It is therefore clear that the amount of unbalance significantly affects the dynamic behavior of the rotor in terms of fluid-induced instabilities. The findings reported here are congruent with the experimental results of Muszynska [11], who demonstrates that higher unbalances produce a wider range of rotations with stable synchronous vibrations, i.e., the subsynchronous vibration is imperceptible.

3.4. Journal-bearing parameters

Other parameters are checked due to their significant influence on the dynamic behavior of the system with respect to hydrodynamic bearings: radial clearance, viscosity of the lubricating oil and L/D ratio (length-to-diameter ratio of the bearing). These parameters are related to the Ocvirk or nondimensional Sommerfeld numbers [14].

However, an analysis of the system's response to the changes in these parameters would not suffice to understand the dynamic behavior of the system, because of the nonlinearities inherent to the rotor-bearing system. Bifurcation diagrams, orbits and Poincaré sections were therefore drawn to illustrate the influence of radial clearance C (Figs. 9 and 10), lubricant viscosity μ (Figs. 11 and 12) and L/D ratio (Figs. 13 and 14).

Increased radial clearance leads to a period-doubling motion, as indicated in Figs. 9 and 10. The transition from a synchronous to a subsynchronous whirl begins when the radial clearance is 80 μm. At a radial clearance of 90 μm, the influence of the half-speed frequency is much higher and at 100 μm the motion is practically period doubling. The same effect is indicated by the viscosity and L/D ratio. Fig. 11 shows the bifurcation

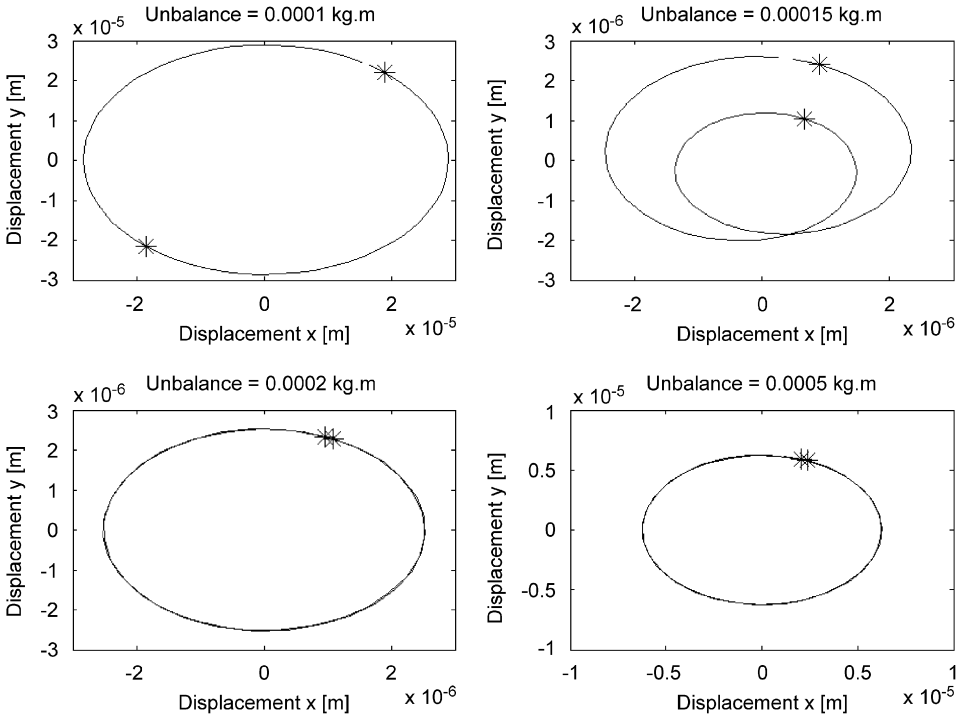

Fig. 8. Orbit and Poincaré sections at 32 Hz for unbalance of 1×10^{-4}, 1.5×10^{-4}, 2×10^{-4} and 5×10^{-4} kg m.

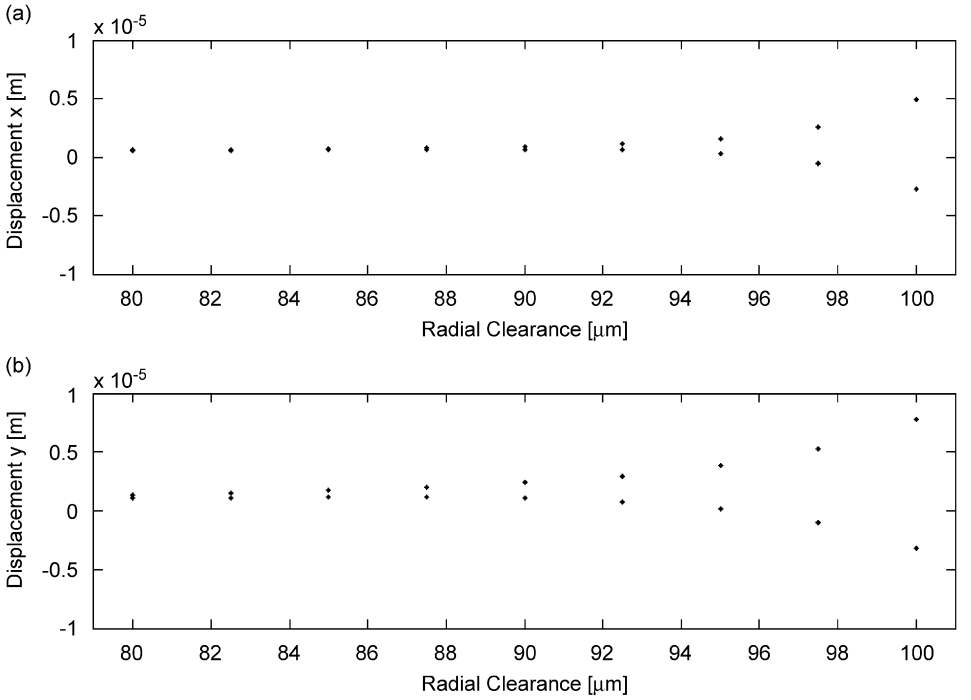

Fig. 9. Bifurcation diagram for influence of radial clearance: (a) horizontal displacement; (b) vertical displacement ($me = 1.5 \times 10^{-4}$ kg m, $L/D = 0.5$ and $\mu = 0.04$ Pa s).

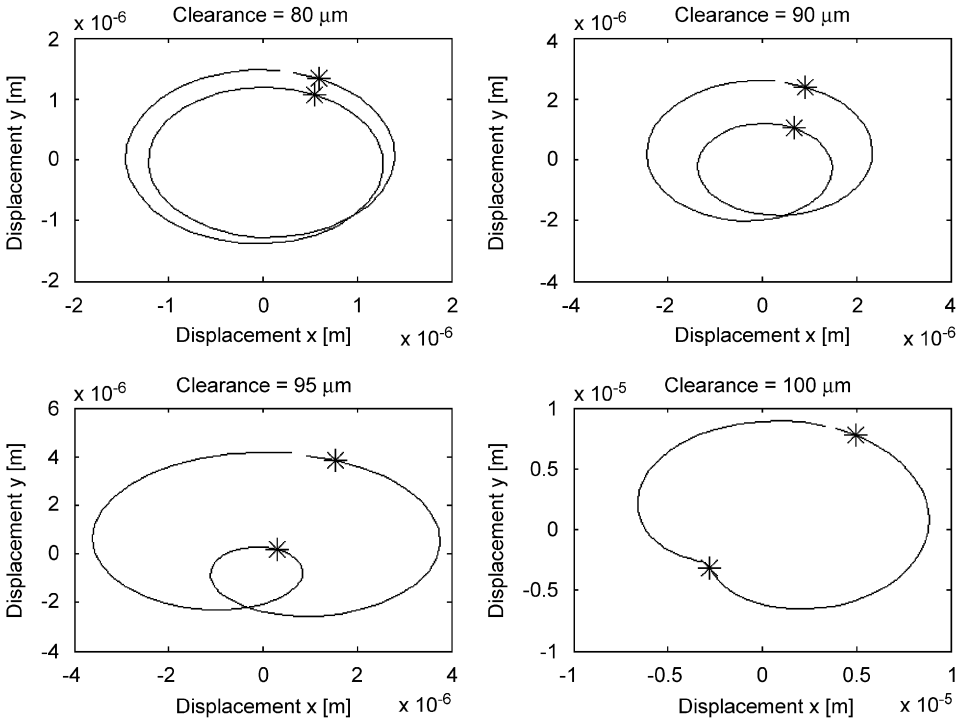

Fig. 10. Orbit and Poincaré sections at 32 Hz for radial clearance of 80, 90, 95 and 100 μm.

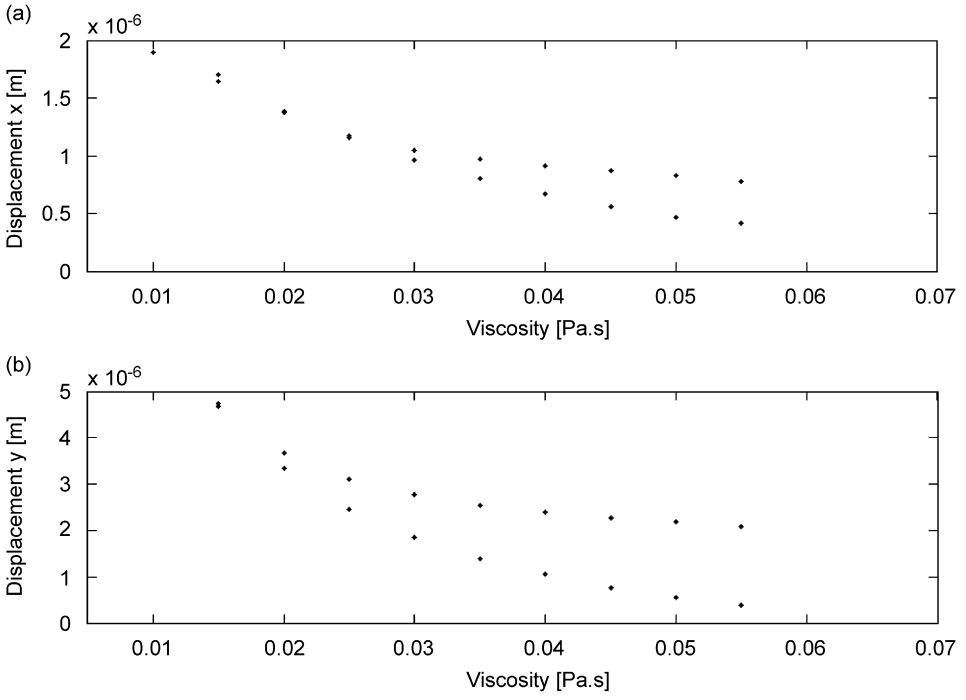

Fig. 11. Bifurcation diagram for influence of viscosity: (a) horizontal displacement; (b) vertical displacement ($C = 90\,\mu m$, $L/D = 0.5$, $me = 1.5 \times 10^{-4}\,kg\,m$).

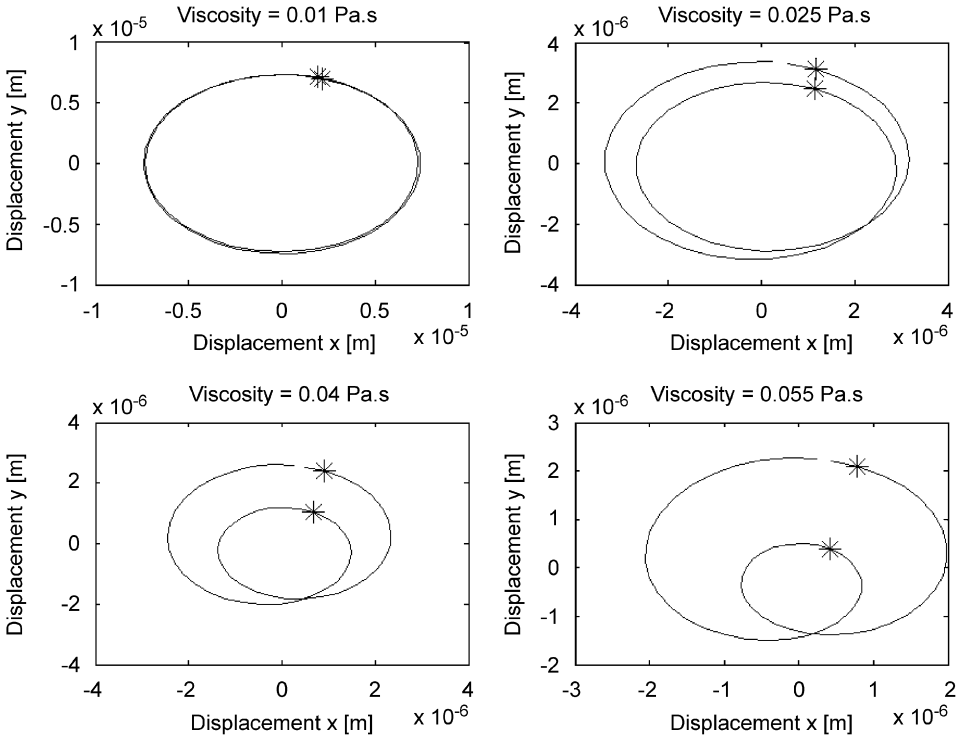

Fig. 12. Orbit and Poincaré sections at 32 Hz for viscosity of 0.010, 0.025, 0.040 and 0.055 Pa s.

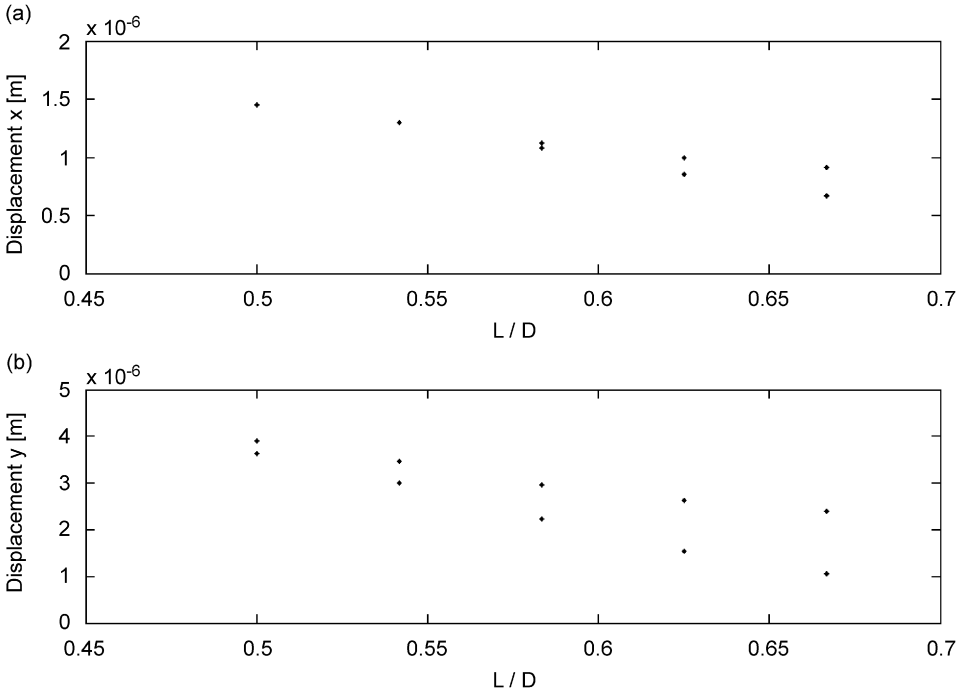

Fig. 13. Bifurcation diagram for L/D ratio: (a) horizontal displacement; (b) vertical displacement ($C = 90\,\mu\text{m}$, $\mu = 0.04\,\text{Pa s}$, $me = 1.5 \times 10^{-4}\,\text{kg m}$).

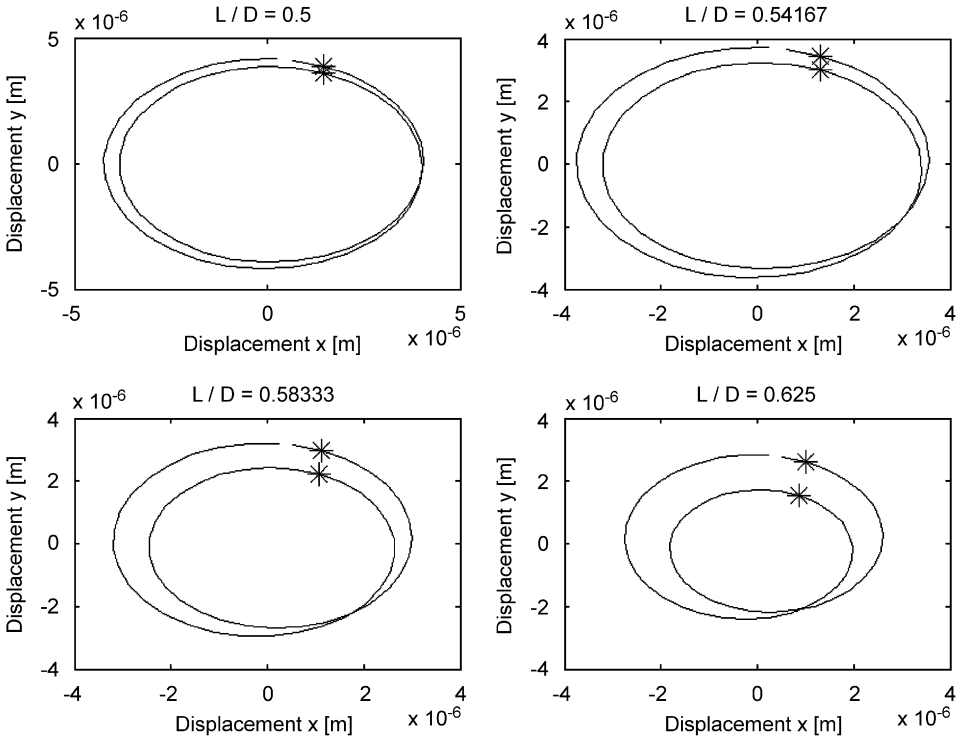

Fig. 14. Orbit and Poincaré sections at 32 Hz for L/D ratio of 0.5, 0.54, 0.58 and 0.625.

diagram and Fig. 12 shows the orbits and Poincaré sections for the variation in viscosity. The motion is synchronous if the viscosity is 0.01 Pa s, but period-doubling motion starts if the viscosity changes to 0.015, indicating the beginning of oil whirl instability. Figs. 13 and 14 show these diagrams for the increase in L/D ratio. At a ratio of 0.5, the unstable motion is at the threshold of instability, showing the transition from synchronous to subsynchronous motion. Another effect that can be observed when the viscosity and L/D ratio increase is the decrease in displacement amplitude, see Figs. 11 and 13. A comparison with Eq. (3) reveals that the higher the viscosity or L/D ratio the higher the hydrodynamic supporting forces. Thus, the stiffness and damping effect are also greater, reducing the amplitude of the displacement.

Therefore, increasing these bearing parameters leads to instable motion, which cannot be determined considering only their relation given by Ocvirk or nondimensional Sommerfeld numbers. The reduction in displacement amplitude due to higher viscosity and L/D ratio is also congruous with these numbers.

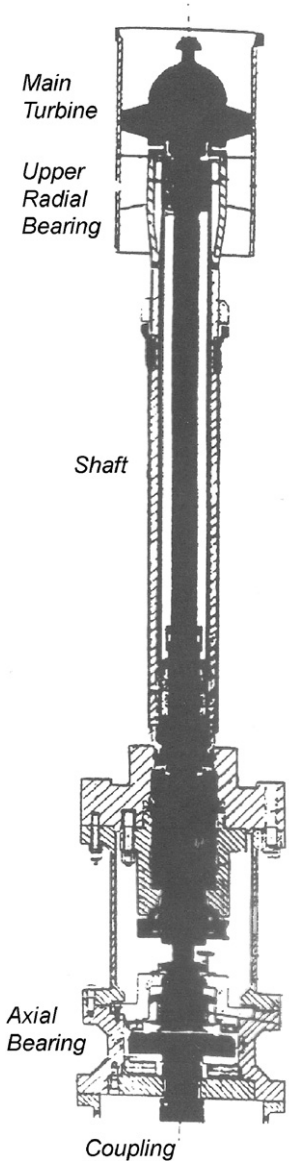

Fig. 15. Schematic of real power plant rotor.

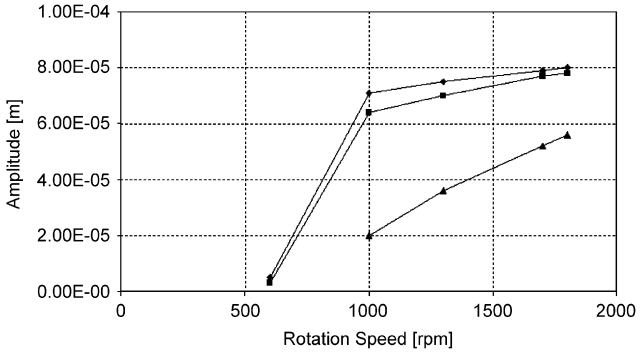

Fig. 16. Unbalance effect of oil-whirl instability in a real turbine (—◆— $Q = 1.5$; —■— $Q = 6.3$; —▲— $Q = 15$).

4. Comparative analysis with a real vertical power plant

The main purpose of the comparative analysis presented here is to illustrate the similarity of the simulated results with measurements taken in a real power plant whose dynamic characteristics closely resemble those of the simulated rotor (Fig. 15). To this end, the behavior of the hydrodynamic cylindrical bearing assembled in the power plant rotor is compared with the computational simulations obtained by the vertical rotor model proposed here. The upper hydrodynamic short bearing is assembled under the main rotor, with a radial clearance of 80 μm. The natural frequency of the rotor is 60 Hz (3600 rev/min), with oil-whip instability at 120 Hz (7200 rev/min).

Fig. 16 shows the influence of the dimensionless unbalance Q (applied unbalance/residual unbalance) on the turbine stability (oil whirl). It is interesting to note the similarity to the simulated results depicted in Fig. 5, except for the effect of the greater flexibility in the simulated rotor, which is revealed by the amplitude peaks at the natural frequency of the rotor (22 Hz). However, one can clearly see that the same unbalance effect occurs in both systems (real turbine and above 35 Hz for simulated rotor): when the mass unbalance increases, the oil whirl is delayed in the frequency domain with lower vibration amplitudes. Therefore, the nonlinear hydrodynamic-bearing model applied here yields very satisfactory results, providing robustness to its application in critical situations, when rotor vibration causes the bearings to work with very thin oil film viscosity.

5. Comparative analysis with a horizontal test rig

The experimental setup consisted of two hydrodynamic bearings and a lumped mass assembled in the center of the shaft (Fig. 17), like the Laval rotor used in the simulation tests. The shaft of the physical system was made of steel with a 12 mm diameter. The distance between the bearings was 600 mm. The concentrated mass consisted of a disk with an external diameter of 94.7 mm, a length of 47.0 mm and a mass of 2.34 kg. A pair of cylindrical hydrodynamic bearings was used to support the shaft, which was made of in bronze, with a radial clearance of 90 μm and L/D ratio of 0.64. The bearings were lubricated with AWS 32 oil, whose operating temperature was close to 25 °C. The nominal frequency of the electric motor lay in the range of 1–60 Hz. The rotor support structure can be considered rigid in these operational frequencies.

The unbalance time response was recorded at the concentrated mass of the rotor. In order to obtain the curves in the horizontal and vertical directions, the orbit of the rotor mass was monitored by two magnetic proximity sensors. To monitor the displacement of the shaft inside the bearings, two magnetic proximity sensors were immersed in the oil film. The measurements were taken within the range of the nominal rotation speed of the electric motor. Fig. 18 shows the variation of the rotation speed over time in a range of 3–50 Hz. A fast runup is carried out first, followed by a slower rundown. The experimental responses (horizontal and vertical directions) are compared with the simulation results. Figs. 19 and 20 show, respectively, the experimental measurements and the simulation results for bearing 1. Figs. 21 and 22 show these results for bearing 2, while Figs. 23 and 24 depict the results for the concentrated mass. In each case, the simulated and

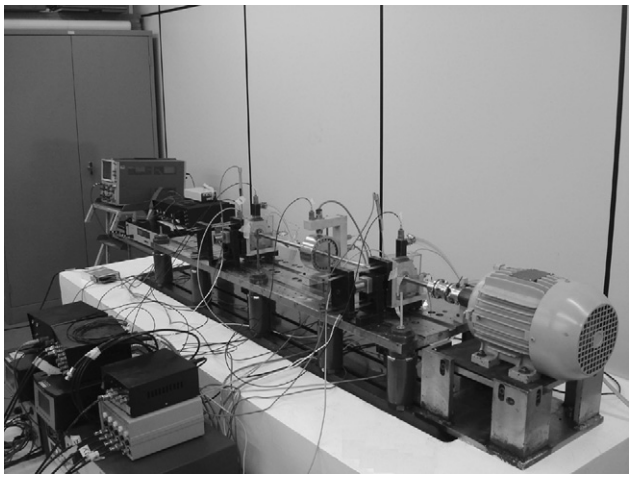

Fig. 17. Experimental test rig.

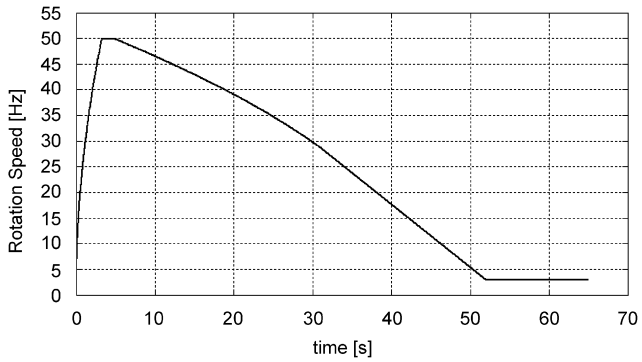

Fig. 18. Variation of rotational speed in experimental data acquisitions.

experimental results are very similar, indicating that the nonlinear journal-bearing model satisfactorily represents the fluid-induced instability effects.

The experimental results of bearings 1 and 2 show a synchronous frequency close to 45 Hz, which is related to the bearing housing first mode shape. Neither this nor the second harmonic effects are taken into account in the numerical simulations.

6. Conclusion

A nonstationary model of a rotor-bearing system is proposed, considering nonlinear hydrodynamic forces. Vertical and horizontal rotors were simulated. Different moments of unbalance were applied to ascertain their influence on the rotor's dynamic behavior and instability threshold. The influence of hydrodynamic journal-bearing parameters such as oil film viscosity, radial clearance and bearing length and diameter ratio were also analyzed.

The bearing's model robust evaluation plays a significant role in the identification processes that involves parallel linear and nonlinear systems. The proposed model is used in numerical simulations of the rotor run up and run down to analyze the dynamic behavior of the bearings. The journal-bearing nonlinear model [2,3] is able to simulate oil whirl and oil whip, showing a promising potential to reproduce displacements and hydrodynamic journal-bearing forces.

The subsynchronous whirl is more evident in the vertical rotor. As shown in Fig. 4b, the oil whirl and oil whip are well characterized. In the horizontal rotor, the whirl instability is not as evident as in the vertical

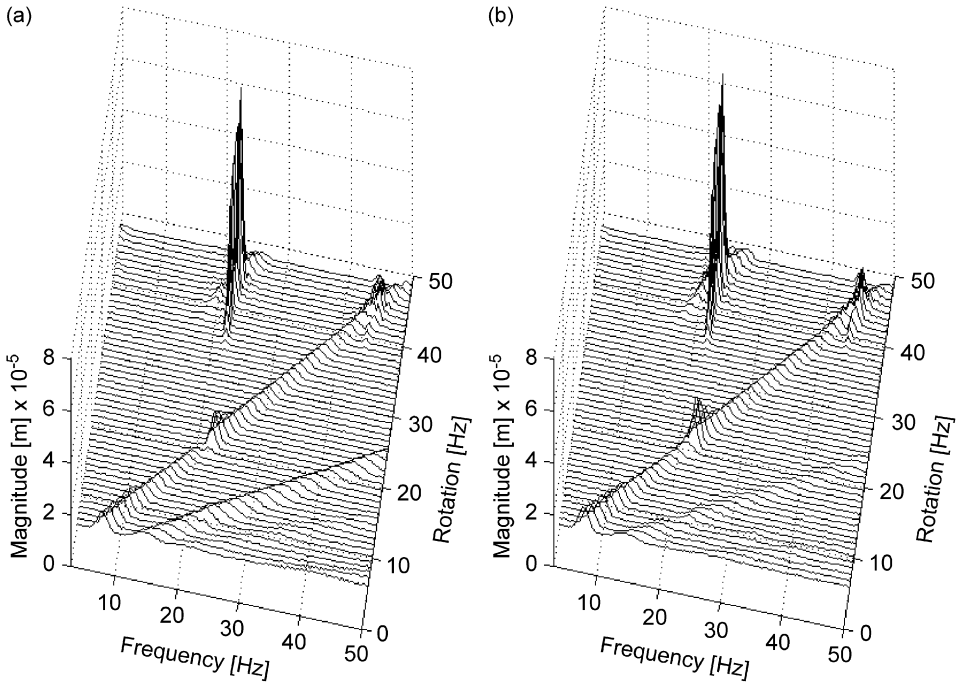

Fig. 19. Experimental results for bearing 1: (a) horizontal displacement; (b) vertical displacement.

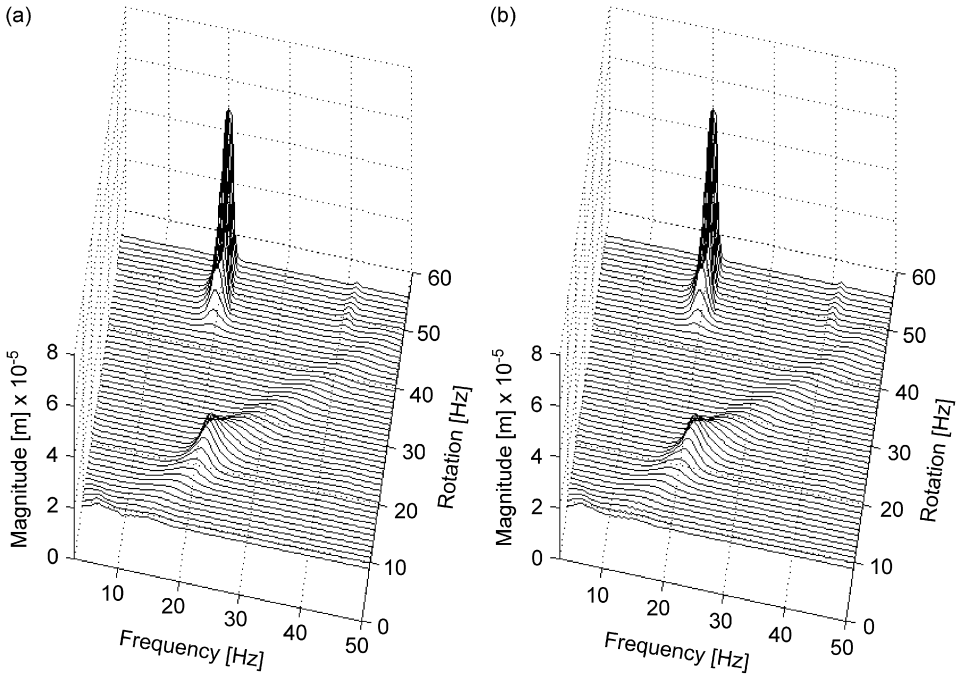

Fig. 20. Simulated results for bearing 1: (a) horizontal displacement; (b) vertical displacement.

rotor, but the whip instability clearly appears at close to double the natural frequency (Fig. 4a). The influence of unbalance was studied in vertical rotors because they highlight the whirl effect. Increasing the moment of unbalance increases the threshold of instability. At the lowest moment of unbalance, synchronous precessional vibration was hardly perceptible in the waterfall plot. As the unbalance moment increased, this kind of

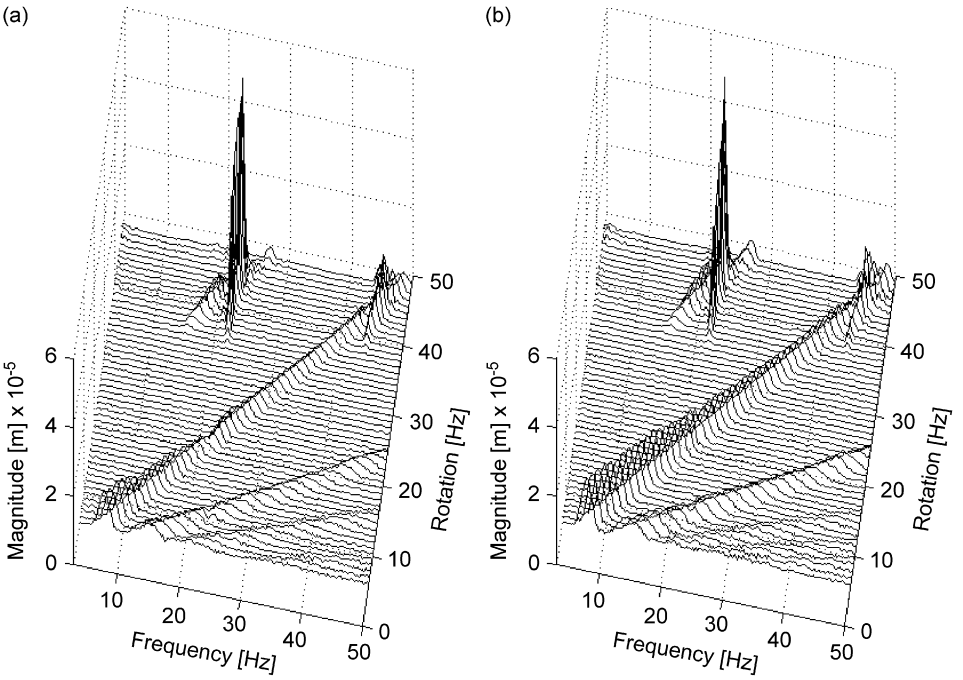

Fig. 21. Experimental results for bearing 2: (a) horizontal displacement; (b) vertical displacement.

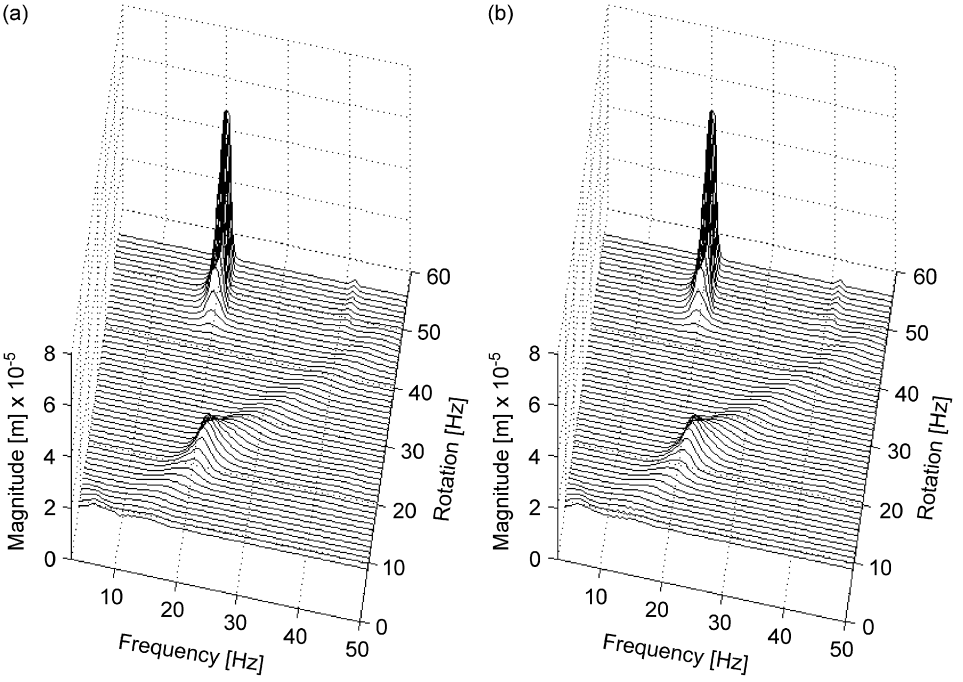

Fig. 22. Simulated results for bearing 2: (a) horizontal displacement; (b) vertical displacement.

vibration became more evident and the region of stability increased. These diagrams are congruent with Muszynska [11,12].

Bifurcation diagrams and Poincaré sections were used to analyze the influence of unbalance and journal-bearing parameters (radial clearance C, viscosity μ and ratio L/D) in the nonlinear dynamic behavior of the

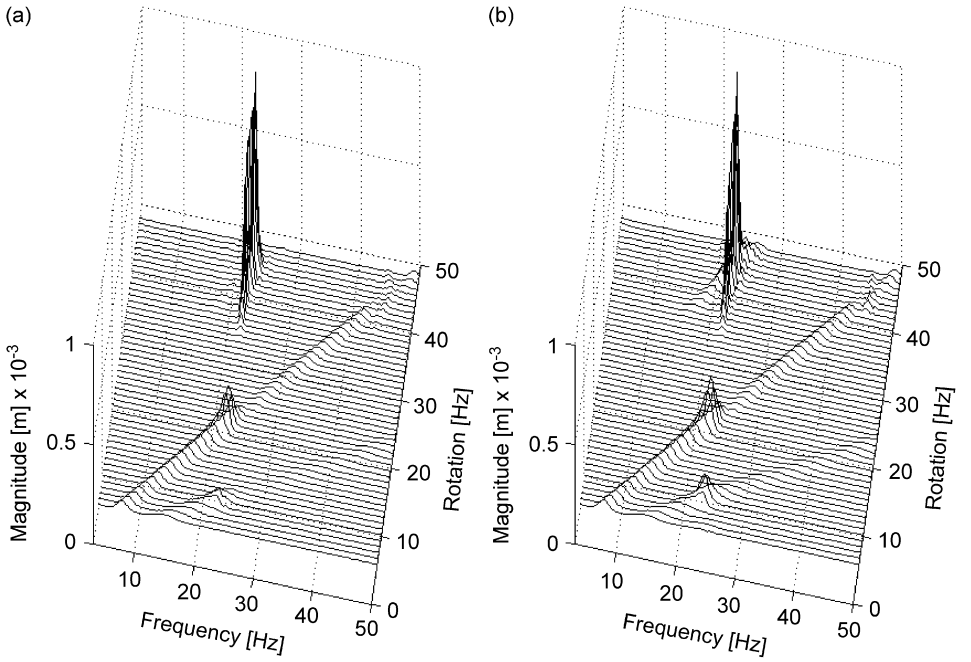

Fig. 23. Experimental results for concentrated mass: (a) horizontal displacement; (b) vertical displacement.

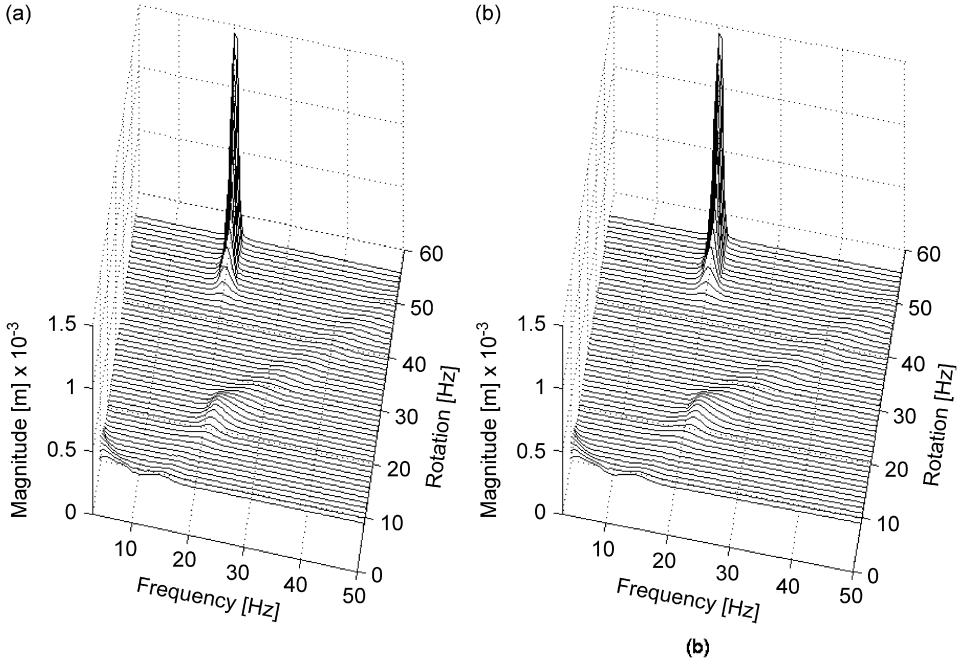

Fig. 24. Simulated results for concentrated mass: (a) horizontal displacement; (b) vertical displacement.

system's response. The decrease of unbalance and increase of all bearing parameters caused a shift from a period motion, characterized by synchronous vibration due to unbalance excitation, to a period-doubling motion, which is characteristic of the half-speed frequency vibration and indicates oil whirl. The orbits and

Poincaré sections show the transition from synchronous to subsynchronous vibration at the threshold of instability.

A comparison was made with a real case study involving a vertical power plant and a horizontal test rig. In the comparison with the vertical power plant, the effect of the unbalance on the oil whirl instability was quite similar to the simulations. Experimental measurements of the test rig were carried out at both bearings and the concentrated mass, showing satisfactory results. This comparison confirmed that the nonlinear hydrodynamic journal bearing model offers a viable solution for rotor-bearing system simulations when considering fluid-induced instabilities.

Acknowledgments

The authors gratefully acknowledge the Brazilian and German research funding agencies CAPES/DAAD PROBRAL program, CNPq and FAPESP for their support of this work.

References

[1] D. Childs, H. Moes, H. Leeuwen, Journal bearing impedance descriptions for rotordynamic applications, *Journal of Lubrification Technology* (1977) 198–214.
[2] G. Capone, Orbital motions of rigid symmetric rotor supported on journal bearings, *La Meccanica Italiana* 199 (1986) 37–46.
[3] G. Capone, Analytical description of fluid-dynamic force field in cylindrical journal bearing, *L'Energia Elettrica* 3 (1991) 105–110 (in Italian).
[4] J.K. Tiwari, A.W. Lees, M.I. Friswell, Identification of speed-dependent bearings parameters, *Journal of Sound and Vibration* 254 (2002) 967–986.
[5] J.K. Sinha, A.W. Lees, M.I. Friswell, Estimating the static load on the fluid bearings of a flexible machine from run-down data, *Mechanical System and Signal Processing* 18 (2004) 1349–1368.
[6] H. Diken, Non-linear vibration analysis and subharmonic whirl frequencies of the Jeffcott rotor model, *Journal of Sound and Vibration* 243 (2001) 117–125.
[7] H.F. Castro, K.L. Cavalca, R. Nordmann, Rotor-bearing system instabilities considering a non-linear hydrodynamic model, *Seventh IFToMM-Conference on Rotor Dynamics*, Vienna, September 2006, pp. 1–10.
[8] K.L. Cavalca, F.G. Dedini, Experimental analysis of tilting-pad journal bearing influence in a vertical rotating system, *IFToMM-International Conference on Rotor Dynamics*, Darmstadt, September 1998, pp. 571–582.
[9] E.P. Okabe, K.L. Cavalca, Rotordynamic analysis if system with a non-linear model of tilting pad bearings, *Seventh IFToMM-Conference on Rotor Dynamics*, Vienna, September 2006, pp. 1–10.
[10] Robert Gasch, Rainer Nordmann, *Herbert Pfützner Rotordynamik*, Springer, Berlin, 2002.
[11] A. Muszynska, Whirl and whip—rotor bearing stability problems, *Journal of Sound and Vibration* 110 (3) (1986) 443–462.
[12] A. Muszynska, Stability of whirl and whip in rotor bearing system, *Journal of Sound and Vibration* 127 (1) (1988) 49–64.
[13] S. Crandall, From whirl to whip in rotordynamics, *Transactions of IFToMM Third International Conference on Rotordynamics*, Lyon, September 1990, pp. 19–26.
[14] Dara Childs, *Turbomachinery Rotordynamics*, Wiley-Intersciences, New York, 1993.
[15] A. Muszynska, D.E. Bently, Fluid-generated instabilities of rotors, *Bently Nevada Corporation ORBIT* 10 (1) (1989) 6–14.
[16] D.E. Bently, The death of whirl and whip, Bently Nevada Corporation ORBIT, Fourth Quarter, 2001, pp. 42–46.
[17] B.-H. Rho, K.-W. Kim, A study of the dynamic characteristic of synchronous controlled hydrodynamic journal bearing, *Tribology International* 35 (2002) 339–345.
[18] J. Jing, G. Meng, Y. Sun, S. Xia, On the non-linear dynamic of a rotor-bearing system, *Journal of Sound and Vibration* 274 (2004) 1031–1044.
[19] J. Jing, G. Meng, Y. Sun, S. Xia, On the whipping of a rotor-bearing system by a continuum model, *Applied Mathematical Modelling* 29 (2004) 461–475.
[20] G. Adiletta, A.R. Guido, C. Rossi, Nonlinear dynamics of a rigid unbalanced rotor in journal bearings—part I: theoretical analysis, *Nonlinear Dynamics* 14 (1997) 57–87.
[21] G. Adiletta, A.R. Guido, C. Rossi, Nonlinear dynamics of a rigid unbalanced rotor in journal bearings—part II: experimental analysis, *Nonlinear Dynamics* 14 (1997) 157–189.
[22] J.K. Wang, M.M. Khonsari, Bifurcation analysis of a flexible rotor supported by two fluid-film journal bearing, *Journal of Tribology* 128 (2006) 594–603.
[23] Q. Ding, A.Y.T. Leung, Numerical and experimental investigation on flexible multi bearing rotor dynamics, *Journal of Vibration and Acoustics* 127 (2005) 408–415.
[24] M.A.C. Michalski, Y.M.B. Moreno, R.O. Rocha, M. Zindeluk, Identifying oil instability phenomena in rotors using nonlinear techniques analysis, *Proceedings of XII International Symposium on Dynamic Problems of Mechanics*, Ilhabela, Brazil, 2007, pp.1–10.

[25] R.L. Ruhl, J.F. Booker, A finite element model for distributed parameter turborotor systems, *Journal of Engineering for Industry* 94 (1972) 128–132.
[26] H.D. Nelson, J.M. McVaugh, Dynamics of rotor-bearing systems using finite elements, *Journal of Engineering for Industry* 98 (1976) 593–600.
[27] K.L. Cavalca, Non-linear analysis of a Laval Rotor passing through the resonance under a Coulomb dry-friction action, *Machine Vibration* 2 (2) (1993) 71–79.